How lowermost mantle viscosity controls the chemical structure of Earth's deep interior

Juliane Dannberg ID[1,+,*], Kiran Chotalia ID[1,+], and Rene Gassmöller ID[1]

[1]Department of Geological Sciences, University of Florida, Gainesville, US
[*]juliane.dannberg@ufl.edu
[+]J.D. and K.C. contributed equally to this work

ABSTRACT

Determining the fate of subducted oceanic crust is critical for understanding material cycling through Earth's deep interior and sources of mantle heterogeneity. A key control on the distribution of subducted slabs over long timescales is the bridgmanite to post-perovskite phase transition in the lowermost mantle, thought to cause rheological weakening. Using high-resolution computational models, we show that the ubiquitous presence of weak post-perovskite at the core-mantle boundary can facilitate or prevent the accumulation of basaltic oceanic crust, depending on the amount of weakening and the crustal thickness. Moderately weak post-perovskite (∼10–100× weaker) facilitates segregation of crust from subducted slabs, increasing basalt accumulation in dense piles. Conversely, very weak post-perovskite (more than 100× weaker) promotes vigorous plumes that entrain more crustal material, decreasing basalt accumulation. Our results reconcile the contradicting conclusions of previous studies and provide insights into the accumulation of subducted crust in the lowermost mantle throughout Earth's history.

Introduction

Under lower mantle conditions, basaltic oceanic crust is expected to have a higher density than the surrounding mantle[1–3]. Therefore, as subducted slabs reach the base of the mantle and heat up, the crust should eventually separate from the lithosphere, sinking down and accumulating at the core-mantle boundary[4,5] (CMB). Geochemical observations support this idea, indicating that some previously subducted crust is recycled back towards the surface in mantle plumes, the sources of ocean island basalt[4,6–10]. The vastly different ages of subducted oceanic crust found in ocean island basalt sources[5]—ranging from as young as 200–650 Ma[11,12] over ∼1.5 Ga[13] to more than 2.45 Ga[9]—imply that crust is not always recycled immediately, but can instead remain in the lower mantle for a substantial amount of time before being brought back to the surface. Seismic tomography models provide insights into where this subducted crust might accumulate. They show two large structures of reduced seismic velocities in the lowermost mantle (the LLSVPs—Large Low Shear Velocity Provinces[14,15], consisting of hot and likely chemically distinct material[16–22] that is intrinsically dense[14,23,24]. These regions are also thought to be plume generation zones[25–27], allowing plumes to carry their geochemical signature towards the surface. All these observations point to the presence of reservoirs in the lowermost mantle where subducted oceanic crust accumulates and is later entrained into rising plumes. However, the degree of basalt accumulation at the base of the mantle relative to entrainment in mantle plumes remains debated[15], and its time evolution needs to be better quantified to advance our understanding of the evolving distribution of subducted oceanic crust in the deep mantle[5].

A key material property controlling the segregation and stirring of mantle material is its viscosity, which decreases drastically near the CMB[28–30]. One reason for this rheological weakening may be the phase transition from bridgmanite to post-perovskite (ppv), reducing the viscosity by 1–4 orders of magnitude[31–33], facilitating more rapid deformation and impacting how subducted slabs interact with the surrounding mantle. However, previous studies on the fate of subducted basaltic crust come to contradicting conclusions: Basalt might be predominantly stirred into the surrounding mantle[34], or it might readily accumulate in thermo-chemical structures at the CMB[35,36]. Weak ppv could further reduce[34], or enhance[35–37], or first increase but later decrease[38] this basalt accumulation, or it might not affect the stability and size of dense reservoirs substantially[39]. This range of predictions shows that the fate of subducted crust is still strongly debated. Because of the differences between these models (see Note S1 for details), their results are not directly comparable, making it impossible to constrain what leads to the different conclusions. Therefore it remains unclear which physical properties of the lowermost mantle affect if and how fast basalt can accumulate in dense piles. Understanding this problem requires a more systematic study with high resolution that can accurately track basaltic material independent of crustal thickness. We here address this controversy by systematically studying the influence of a ubiquitous weak ppv layer above the CMB using an adaptive finite-element grid and a modern particle method for tracking chemical heterogeneities.

Results and Discussion

Impact of the slab density structure

To explain the discrepancies between previous studies, we first investigate the impact of the slab density structure on basalt accumulation. We set up models with the density contrasts between basalt, pyrolite and harzburgite taken from (i) Tackley (2011)/Nakagawa & Tackley (2011)[35,36], (ii) Li & McNamara (2013)[34], and (iii) thermodynamic data computed with HeFESTo[3], and otherwise use all parameters from[36]. This allows for a direct comparison between studies. Our results (Figure S1, Movies S1 to S6) show that all models accumulate basalt at the CMB, with only slight changes in accumulation rate due to different densities. Despite the density contrast between basalt and pyrolite being doubled in[35] compared to HeFESTo, both models behave almost identically. The[34] setup results in slightly faster basalt accumulation because it does not include a harzburgitic lithosphere and therefore features comparatively heavier slabs. These cold slabs remain at the CMB for a longer time, allowing for easier segregation of basalt from the slab and suppressing plume formation and entrainment of basalt (see Figure S2).

A weak ppv phase (Figure S1, dashed lines vs solid lines) affects basalt accumulation much more drastically, increasing it by a factor of 2–3. This general trend is consistent with[35,36], the studies the model setup is based on. However, these models highlight that the density—often assumed to be the most important parameter for basalt accumulation[5]—is not the reason for the discrepancies between previous studies and that instead other factors such as the lowermost mantle viscosity may be more important.

Impact of post-perovskite viscosity on basalt segregation

In order to better understand the controls on basaltic pile formation in the Earth's mantle, we therefore systematically test the effects of lowermost mantle viscosity and slab thickness in models with realistic densities from a mineral physics database[3]. Specifically, we vary the viscosity contrast across the bridgmanite to ppv transition, and the thickness of subducted oceanic crust, which has been shown to strongly affect its ability to accumulate on the CMB, with a thicker crust making accumulation more likely[34,38].

We start our models with two subducted slabs entering from the top, and no basalt near the CMB. For a crustal thickness of 30 km in the lower mantle, if no change in viscosity is associated with ppv (No viscosity reduction in Figure 1a), most crustal material entering the CMB region is immediately entrained into mantle plumes and being carried back towards the surface. However, if the viscosity of ppv is 100× lower, crustal material easily segregates from the slab and accumulates at the base of rising plumes (Weak post-perovskite in Figure 1b). This is because a weak ppv layer allows the slab as a whole and oceanic crust specifically to penetrate the thermal boundary layer at the base of the mantle more easily, an effect that is particularly important if the slab overturns and the crust directly impinges on the CMB (i.e., 100 Myr panel in Figure 1b vs. 400 Myr panel in Figure 1a). The crust can then be swept towards the base of plumes and accumulate in dense piles. But even if the slab does not overturn, its lowered viscosity due to the presence of weak ppv facilitates internal deformation of the slab so that the dense basaltic crust can separate from the lighter harzburgitic layer and sink to the CMB (i.e., 200 Myr panel in Figure 1b). The combined effect causes basalt accumulation at the CMB to approximately double in the model with 100× weaker ppv compared to the model without weakening (see Figure 1c, 100× vs. no viscosity reduction).

Rate of basalt accumulation

Figure 1c shows that this trend changes throughout the model evolution across the range of tested ppv viscosities. During the first 70 million years, lower ppv viscosity consistently causes faster basalt accumulation. In later stages however, the mass of basaltic piles remains approximately constant in models with weak ppv, and the transition from growth to steady-state occurs earlier the lower the ppv viscosity. This indicates that while low ppv viscosity enhances the segregation of oceanic crust from the slab (a process that is active from the start of the model and remains active throughout its whole evolution), it can also facilitate mantle processes that later limit the growth of existing basaltic piles (such as the entrainment of pile material into upwards mantle flow). These processes lower the volume of basaltic piles after 400 Myrs of accumulation substantially if ppv is 1000× weaker than bridgmanite compared to the models with a viscosity reduction of only 10× or 100×. On the other hand, increasing the crustal thickness at a given ppv viscosity consistently increases the rate and steady-state value of basalt accumulation (Figure 1d) in agreement with previous studies[34,38].

To understand this dependence of basalt accumulation on both ppv viscosity and oceanic crustal thickness, we compare the amount of basalt after 400 Myr of accumulation for all different parameter combinations (Figures 2 and 3). Only in some models, basaltic piles form at the base of mantle plumes, while in others, almost all basaltic material is entrained into upwards mantle flow rather than remaining at the CMB (Figure 2). Quantifying the amount of basalt in the lowermost 300 km of the mantle at the end of each model (Figure 3a) highlights the distinct impact of the two model parameters. While an increasing crustal thickness (going upwards in each column) consistently increases the amount of basalt accumulating near the CMB, the influence of the ppv viscosity is more complex. Compared to models with no ppv viscosity reduction, a small amount of weakening (going from right to left in each row) increases how much basalt accumulates. However, further weakening of ppv

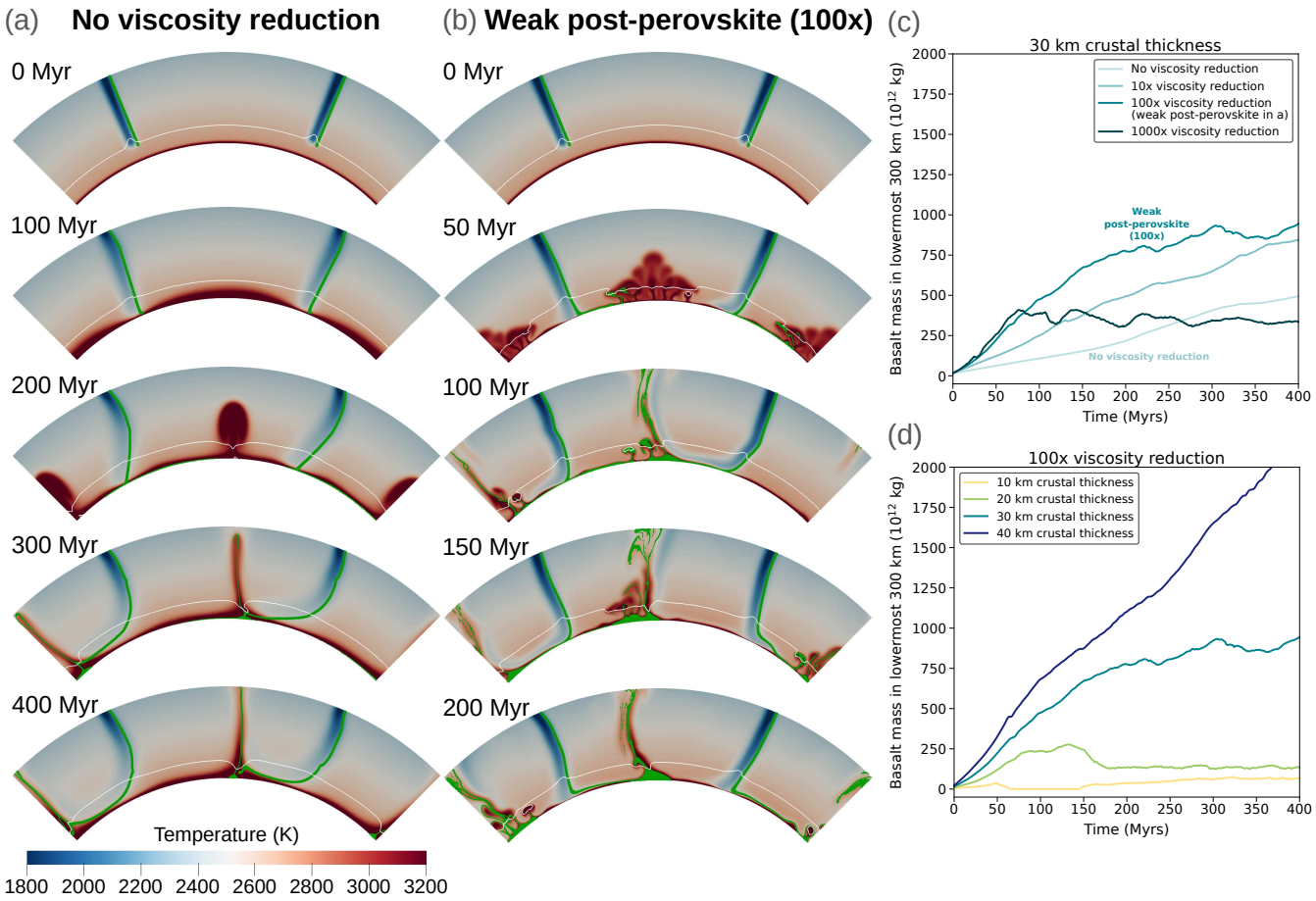

Figure 1. Changes in basalt accumulation over time. (a, b) Model evolution with unchanged (a) and 100× weaker (b) ppv and 30 km crustal thickness. Blue-to-red background colors illustrate temperature, green colors indicate presence of basalt, white line marks the ppv phase transition. (c, d) Evolution of the amount of basalt in the lowermost 300 km of the mantle, for a crustal thickness of 30 km and different ppv viscosities (c), and for a ppv weakening factor of 100 and different crustal thicknesses (d). Lines representing the models in (a) and (b) are annotated.

reverses this trend, lowering the amount of basalt in the CMB region. The viscosity at which this reversal occurs increases with crustal thickness. The most basaltic material accumulates for intermediate ppv weakening and large crustal thickness (40 km, 100× weaker).

Basalt segregation vs. entrainment

We interpret this behavior as the result of two competing processes: The lower the ppv viscosity and the thicker the crust, the easier it is for basalt to segregate from the slab (see also Note S2 and Figures S5 and S6). Both factors increase the downward buoyancy forces of the dense basaltic crust compared to the viscous forces resisting segregation. But the lower the ppv viscosity and the thinner the crust and therefore the subducted slabs, the more vigorous are the rising plumes. One reason for this relationship is that thicker slabs bring more cold material to the CMB, suppressing plume formation, whereas thinner slabs heat up faster and allow for more plumes. Alternatively, we can also consider the ppv phase as a separate convecting system with its own Rayleigh number. Computing this number for our model parameters (see Table S1 and Figure S7) without any weakening effect gives approximately 250, below critical, and no internal convection is expected to occur. Since the Rayleigh number is inversely proportional to the layer viscosity, weaker ppv increases the Rayleigh number, and all weakening factors we used (10 to 1000) would allow for internal convection within the layer. The weaker the ppv, the more vigorous the convection, leading to a more efficient heat transport out of this layer and into plumes. Therefore both a thin crust and a weak ppv phase facilitate plume formation and lead to more entrainment of basalt in upwards flow. This effect becomes apparent in the large-scale flow patterns as well (Figure 2): Strong upwellings (low ppv viscosity, thin crust) change the convective planform to only have one subducted slab (panels a–d, g, h), whereas fast accumulation of basalt (intermediate ppv viscosity, thick crust) can suppress the

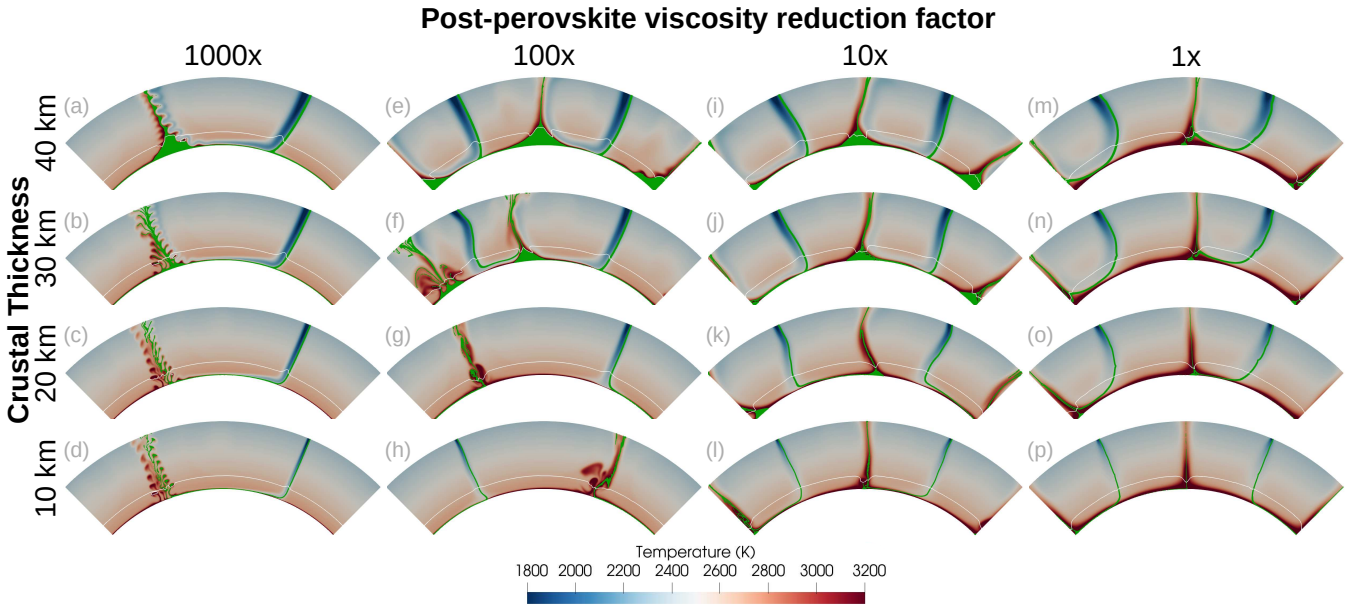

Figure 2. Basaltic accumulation at the end of the model evolution after 400 Myr. Blue-to-red background colors illustrate temperature, green colors indicate presence of basalt. White line marks the ppv phase transition. Full model evolution is shown in Movies S7–22.

formation of strong plumes (panels e, i, j).

Only if basalt segregation is fast and entrainment in plumes is low, thermochemical structures at the CMB can grow efficiently. To estimate under which conditions this is the case, we can analyze the timescales of these processes (Figure 4). In its simplest form, basalt segregation can be considered as an instability of an interface between two materials of different densities, i.e. a Rayleigh–Taylor instability. The characteristic growth time of such an instability[40] (Figure 4a) is

$$\tau_{\text{seg}} = \frac{13.04\eta_{\text{ppv}}}{\Delta\rho g h} \tag{1}$$

where η_{ppv} is the ppv viscosity, $\Delta\rho$ is the density difference between basalt and pyrolite, g ist the gravitational acceleration, and h is the crustal thickness. Basalt can segregate if the crustal layer becomes unstable before it is carried back upwards with the large-scale mantle flow, or in other words, if the growth time is small compared to the characteristic time scale of convection. We can approximate this time as

$$\tau_{\text{conv}} = \frac{s_{\text{con}}}{u_{\text{con}}} = \frac{\pi r_{\text{CMB}}}{4 n_{\text{plumes}} u_{\text{con}}} \tag{2}$$

where u_{con} is the characteristic speed of convection and s_{con} is a characteristic distance between downwellings and upwellings, which in our models can be approximated as $s_{\text{con}} = 2\pi r_{\text{CMB}}/(8 n_{\text{plumes}})$ (with r_{CMB} being the radius of the CMB and n_{plumes} the number of plumes in a given model). The factor of 8 arises because our model geometry is a quarter spherical shell, and the distance between upwellings and downwellings is half the distance between two plumes. However, segregated basalt will only remain at the base of the mantle if this characteristic time scale of convection is short compared to the onset time of thermochemical plumes τ_{plume} (Figure 4b), which can be calculated by solving the equation[41]

$$\text{Ra}_{\text{crit}} = \frac{\rho\alpha g \Delta T(\delta - h)^3}{\eta_{\text{ppv}}\kappa}\left(1 - \frac{h}{\delta}\right) \tag{3}$$

for the critical thickness of the thermal boundary layer δ, given the density ρ, the thermal expansivity α, the temperature contrast ΔT across the thermal boundary layer at the CMB, and the thermal conductivity κ. Note that this approximation is only valid as long as the basaltic layer does not convect internally. Using the solution for δ from (3), the breakaway time of a plume[40] is then calculated as $\tau_{\text{plume}} \approx 0.185\delta^2\kappa^{-1}$. Only if $\tau_{\text{seg}} \lesssim \tau_{\text{conv}} \lesssim \tau_{\text{plume}}$, basalt can accumulate effectively at the base of the mantle.

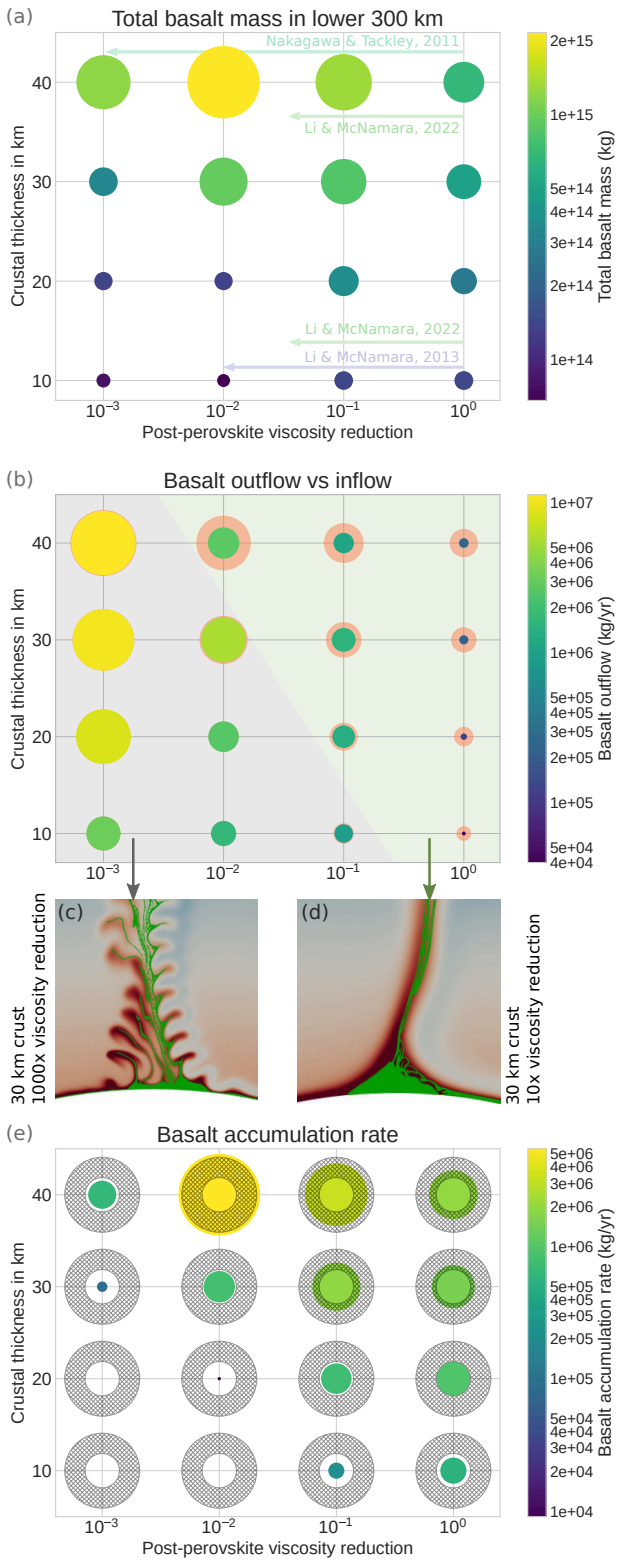

Figure 3. Basalt inflow, outflow, and accumulation rates. (a) Basalt accumulation in the lowermost 300 km of the model after 400 Myr of evolution. Circle size and color indicate basalt mass. (b) Flow of basalt out of the model, averaged over the last 200 Myr of model evolution (colored circles), compared to the basalt inflow (orange circles). Circle sizes indicate inflow/outflow rates. In models with more inflow than outflow (indicated by the orange rims) basalt steadily accumulates at the CMB. (c, d) Example plume morphologies for the two regimes inflow=outflow (c) and inflow>outflow (d). (e) Rate of basalt accumulation at the CMB, averaged over the last 200 Myrs of model evolution. Rings with criss-cross pattern mark the minimum and maximum rate allowed to grow the basaltic piles to a volume comparable to today's LLSVPs, so that models where the radius of the colored circle falls between the inner and outer radius of the shaded ring match observations.

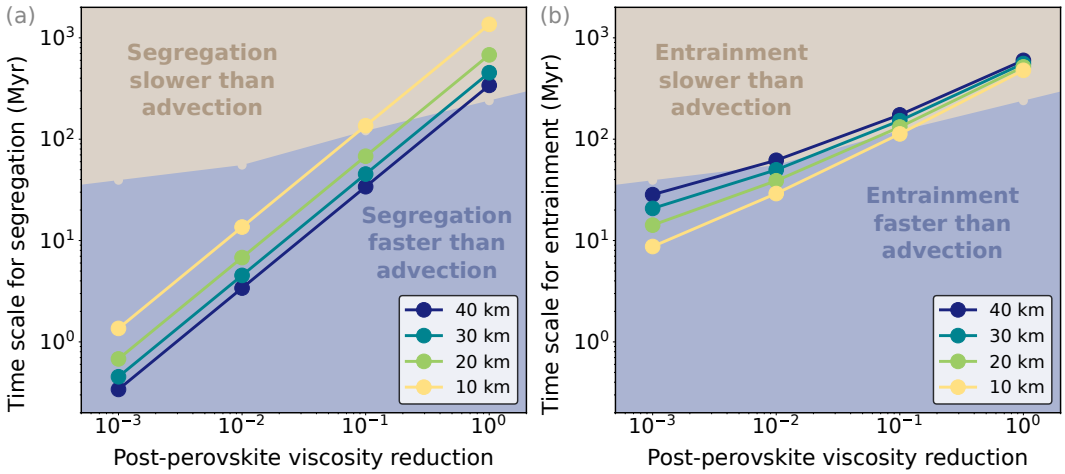

Figure 4. Analytically estimated characteristic time scales of basalt segregation, transport and entrainment. (a) Time scales of segregation of basaltic crust τ_{seg} and (b) onset of thermo-chemical plumes τ_{plume} for different crustal thicknesses (indicated by line colors) are compared to the time it takes for the basaltic layer to be transported along the CMB from a downwelling to an upwelling (τ_{conv}, interface between blue and brown background colors). All parameters are given in Table S2.

This effect is illustrated in Figure 3b, which compares the flow of basalt into and out of the model throughout the last 200 Myr of its evolution: For weak ppv and thin crust (small τ_{plume}), entrainment of basalt in plumes is so efficient that the inflow and outflow are equal. In this case, as much basalt is brought to the CMB region by subducted slabs as is carried upwards again, and basalt accumulates only in a short initial phase (see also Figures S3, S4). While this allows some small basaltic piles to form at the base of plumes (Figure 2), these piles do not continue to grow over time. On the other hand, for thick crust and high ppv viscosities (large τ_{plume}), the inflow is larger than the outflow, allowing for consistent basalt accumulation at the CMB over time. But high ppv viscosities do not allow basalt to segregate fast enough to efficiently accumulate at the CMB (large τ_{seg}). Therefore, the growth rate of these basaltic piles generally increases with decreasing ppv viscosity (Figure S4) until ppv is weak enough that basalt entrainment into plumes becomes so efficient that it compensates the increased basalt inflow due to faster segregation. This compensation also indicates the change in trends from an increased size of basaltic piles for lower ppv viscosity to a reduced size (for any given crustal thickness, as shown in Figure 3a,b). Therefore, there is an optimum value of the ppv viscosity that allows for the fastest growth of basaltic structures at the CMB, with the specific value depending on the crustal thickness.

Dynamically, this compensation between basalt inflow and outflow occurs when the thermal boundary layer at the CMB becomes convectively unstable in the time it takes basaltic material to laterally move from where slabs impinge on the CMB to where plumes rise ($\tau_{conv} > \tau_{plume}$, see Figure 4b). This instability manifests as small plumes rising within the ppv layer that move towards and merge within the upwellings that are part of the large-scale mantle flow system (Figure 2, 3b,c,d). Because the smaller thermal instabilities within the ppv layer have to push through the crustal layer of the subducted slab to rise, they transport basaltic material upwards and facilitate its entrainment in the larger-scale upwellings. Without these instabilities, basaltic material can more easily accumulate at the base of large upwellings where the flow converges. Therefore, small-scale instabilities of the thermal boundary layer dramatically increase the amount of basalt being transported away from the CMB. The effect is also visible in the plume morphology in Figure 2: In models where plumes feature internal thermal heterogeneities resulting from the merging of smaller plumes ($\tau_{conv} > \tau_{plume}$), basalt inflow is compensated by outflow (grey area in Figure 3b). Conversely, in models where temperatures in the plume conduit gradually decrease from the center outwards with no smaller-scale internal structure ($\tau_{conv} < \tau_{plume}$, the basalt inflow substantially exceeds the outflow (green area in Figure 3b). The growth rate of these instabilities depends both on ppv viscosity (lower viscosities increase the internal Rayleigh number of the ppv layer) and the crustal/slab thickness (thicker slabs bring more cold and dense material towards the CMB, increasing the time it takes to heat up enough material to form a plume), explaining the changing trends in basalt accumulation throughout the whole parameter space.

Our analysis also explains why previous studies came to strikingly different conclusions on the effect of low-viscosity ppv. One[34] uses a low crustal thickness (6 km at the surface, 9 km at the top of the lower mantle) and a viscosity reduction factor of 100. Therefore, the model with weak ppv crosses into the part of the parameter space where entrainment in plumes is strong and prevents basalt accumulation (Figures 2d, h, l, p and 3a). Conversely, other models[35] feature a thick crust (limited by the ~45 km model resolution) and a viscosity reduction factor of 1000. For this parameter combination, the enhanced segregation

due to weaker ppv still dominates and leads to more basalt accumulation (Figures 2a, e, i, m and 3a). A third set of models[38] feature a crustal thickness that decreases from 40 to 10 km over time and ppv that is weaker by a factor of 50, explaining the finding that at first, weak ppv causes faster basalt accumulation, but eventually leads to increased entrainment and smaller basaltic piles. Our study therefore reconciles the contradictory results of previous models and provides a framework for how to interpret their conclusions. Note, however, that this analysis (both in our and previous studies) depends on the assumption that there is a ubiquitous layer of ppv above the CMB, which is still debated (for a detailed discussion, see the Model limitations section in the Methods). In the following, we discuss the plausibility of our results using observational constraints and derive consequences for Earth's evolution.

Plume morphology

The merging of smaller plumes into larger upwellings at low ppv viscosities also causes periodic variations in plume volume flux visible as pulses within the modeled plume conduits. Such pulses have previously been suggested for the Iceland plume based on observations of V-shaped ridges propagating outward from the Mid-Atlantic Ridge and away from Iceland. These ridges are thought to result from temporal variations in melt production rate due to variations in plume temperature[42–44]. Early estimates[44] constrain the principal pulse time scale to 5–6 Myr, with a superimposed scale of 2–3 Myr and temperature variations of 30–35 K. A later study[45] finds that between 55 and 35 Ma, small (5–10 K) fluctuations of plume temperature have a periodicity of ∼3 Myr, and after 35 Ma, fluctuations of plume temperature became larger (∼25–30 K) and have a periodicity of up to 8 Myr. The authors propose that the periodicity is caused by boundary layer perturbations within the convecting mantle.

To compare the periodicity in our models to these observations, we compute a power spectrum of the plume temperature in the last 150 Myr of model evolution using a Fourier transform (Figures S8 and S9). This choice of time interval ensures plumes are present in all models. The analysis shows that both higher ppv viscosity and thicker subducted crust shift the spectral energy towards lower frequency (longer time periods), with the viscosity having the stronger effect. For the lowest values of both model parameters, dominant frequencies approach 2 Myr and are therefore near the minimum of what we can resolve with our output time interval of 1 Myr. However, we confirmed in the graphical output (see Figure 2) based on the distance between plume pulses and the upwelling velocity of the plumes, that the periodicity is in the range of 1.7–2 Myr. For the highest viscosity values, the periodicity approaches the averaging interval of 150 Myr. To match the observations and develop a 5–6 Myr (and potentially 2–3 Myr) period, the viscosity reduction caused by ppv would likely need to be 2 to 3 orders of magnitude. Interestingly, as outlined above, models with these viscosities accumulate basalt near the CMB only for large values of crustal thickness of ∼40 km. Therefore, if the periodicity in the Icelandic plume is caused by temperature variations embedded into the plume at the CMB, this would require both a moderate to low ppv viscosity (reduction of a factor 100–1000) and a large crustal/slab thickness near the CMB. Determining if plume pulsations can indeed act as a window into CMB processes would require additional observations of the variability of hotspot activity and a more focused modeling study.

Growth of basaltic piles throughout Earth's history

To compare the volume of basaltic piles predicted in our models to the observed LLSVP volume—estimated to be between 1.6%[27] and 8%[46] of the mantle volume—we extrapolate the basalt accumulation rate from the last 200 Myrs of model evolution throughout Earth's history. This extrapolation is only a first-order approximation, which assumes a constant accumulation rate over a time period of 3 Gyrs, and that our models also apply to Earth's 3D geometry. Keeping these limitations in mind, our analysis (Figure 3e) shows that in models with at least 30 km crustal thickness and 1–10× ppv viscosity reduction the amount of basalt accumulating at the CMB matches the observed LLSVPs. However, this estimate has large uncertainties and the LLSVPs are unlikely to consist entirely of subducted crust but rather a mixture of different materials. Therefore, lower accumulation rates, such as in the models with 30 km crustal thickness and 100× viscosity reduction, or 20 km crustal thickness and 1–10× ppv viscosity reduction, can also be considered as feasible scenarios. Conversely, all models with both low ppv viscosities and low crustal thickness (bottom left in Figure 3c) have minimal accumulation rates that would make it unlikely for old recycled material to be so closely associated with plumes. Note that the model with the maximum accumulation rate (40 km thickness, 100× viscosity reduction) over-predicts the observed LLSVP volume.

Considering that the basalt accumulation rate likely changed over Earth's history, we can use our models to discuss general trends of this change. Our results show, in agreement with previous studies[5], that the oceanic crustal thickness governs the efficiency of basalt accumulation at the base of the mantle. One source of variability for this incoming oceanic crustal thickness is the transition of slabs from the upper to the lower mantle (outlined in the Methods), another source is mantle temperature. Higher temperatures in Earth's past likely led to more partial melting at mid-ocean ridges and therefore to the formation of thicker oceanic crust[47]. Furthermore, the presence of a layer of dense material at the base of the mantle created by differentiation processes early in Earth's history would have facilitated basalt segregation from slabs[36]. Consequently, one might assume that most basalt accumulation occurred early after the onset of subduction[38]. However, while higher mantle temperatures likely support segregation of crust, they would also decrease the mantle viscosity and therefore increase its Rayleigh number. Viscosity affects both segregation and entrainment, making its overall effect on basalt accumulation difficult to predict[5]. In

addition, the thickness of the ppv layer would be reduced in a hotter mantle due to the strong positive Clapeyron slope of its phase transition (visible in plumes in Figure 2). Ppv may not have been stable in hot regions, or only formed a very thin layer above the CMB. Therefore, the relationship between weaker ppv and increased basalt entrainment might not be valid earlier in Earth's history. However, since cold subducted slabs would still undergo the transition to ppv, it is likely that the weakening effect would still facilitate basalt segregation. While the complexity of all processes involved make it difficult to predict the exact effects of an increased mantle temperature without models tailored to this question, both the increased crustal thickness and the diminished presence of ppv in hot regions make it likely that basalt accumulation would have been faster in the past compared to today. This also has implications for the thermal evolution of the Earth, since the accumulation of basaltic material at the CMB can have an insulating effect on the core[48,49].

Methods

We compute our models using the geodynamic modeling software ASPECT[50–54]. We solve the equations for compressible mantle convection, considering only viscous stresses, and assume that the viscosity is isotropic and the material is near-incompressible, making the bulk viscosity very small[40]. Specifically, we formulate the conservation equations for mass, momentum and energy as follows:

$$-\nabla \cdot (2\eta \dot{\varepsilon}) + \nabla p = \rho \mathbf{g}, \tag{4}$$

$$\nabla \cdot (\rho \mathbf{u}) = 0, \tag{5}$$

$$\rho C_p \left(\frac{\partial T}{\partial t} + \mathbf{u} \cdot \nabla T \right) - \nabla \cdot (k \nabla T) = \rho Q + 2\eta \dot{\varepsilon} : \dot{\varepsilon} + \alpha T \mathbf{u} \cdot \nabla p \tag{6}$$

where $\mathbf{u}$ is the velocity, $\dot{\varepsilon}$ is the deviatoric strain rate, p the pressure and T the temperature. Additionally, η is the viscosity, ρ is the density, $\mathbf{g}$ is the gravity vector, C_p is the specific heat capacity of the material, k is the thermal conductivity, Q is the intrinsic specific heat production, and α is the thermal expansion coefficient. All material properties may depend on the current temperature and pressure.

To minimize numerical diffusion, we use particles[52] to track the evolution of the chemical composition. Specifically, our model contains three distinct compositions, namely, pyrolite, harzburgite and mid-ocean ridge basalt. We assign each particle a composition in terms of the fraction of each of pyrolite, harzburgite or basalt according to the initial conditions, or the boundary conditions in case of particles entering the model at a later point. Throughout the model evolution, we interpolate from the particles to the finite-element grid using a bilinear least squares interpolator that includes a global limiter constraining the compositions between 0 and 1. We advect the particles using a second-order Runge–Kutta scheme[55]. To accurately track the composition, we set a minimum number of 20 particles per cell, enforced by adding new particles with properties being initialized using the bilinear least squares interpolator discussed above. To keep computational times tractable, we also enforce a maximum limit of 320 particles per cell. This is necessary because an adaptive mesh (see Geometry section) can drastically shift the number of particles within a cell; the value is chosen as 16 times the minimum number of particles to allow for two levels of mesh refinement/coarsening without addition or deletion of particles. These parameters lead to approximately 11 million particles per model.

Geometry

The model domain (Figure 5) is a quarter of a spherical shell of the lower half of the mantle, extending 1500 km upwards from the CMB to the mid-mantle. Therefore the model only contains one major mantle phase transition: from bridgmanite to ppv.

Using a 2D model focused on the lower mantle allows us to achieve the required high resolution to model basalt segregation in a low-viscosity layer. Specifically, we use an adaptive finite-element mesh to discretize the model domain with a cell size between 4 and 12 km (depending on the refinement level and distance from the CMB). To accurately track recycled material and to make sure we resolve convective processes in the low-viscosity layer at the CMB, we refine the mesh wherever the fraction of basalt or ppv is higher than 10%. Since we use second-order finite elements for velocity, we achieve a resolution of 2 km in horizontal and 3 km in vertical direction in terms of distance between the quadrature points in the low-viscosity layer above the CMB.

Equation of State

We compute the density, thermal expansivity and specific heat from look-up tables created with the global Gibbs free energy minimization code HeFESTo[3,56,57] for three distinct chemical compositions[58]: pyrolite, harzburgite, and mid-ocean ridge basalt (see Figure S7). These material properties already include the effects of compressibility and phase transitions. If a cell in our model contains a mix of these endmember compositions, we assume a mechanical mixture and arithmetically average the material properties (based on a composition's volume fraction for density and thermal expansivity, and based on mass fractions for the specific heat). For simplicity, we use a constant thermal conductivity of 9 W m^{-1} K^{-1}[59].

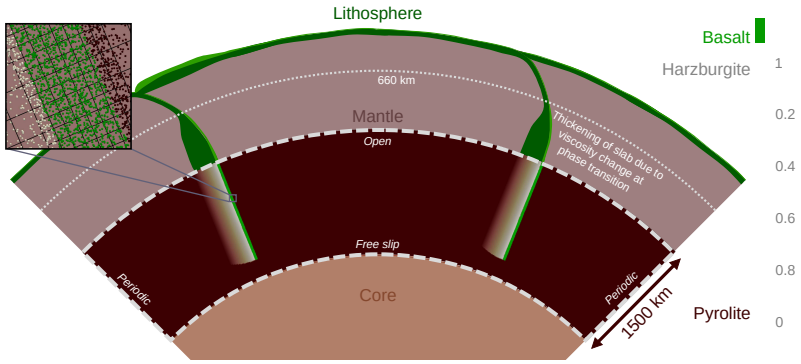

Figure 5. Model setup. Our model includes the lower 1500 km of the mantle (inside the dashed white line). The open top boundary allows two slabs with a prescribed temperature and composition to enter the model. Colors within the white dashed outline illustrate the initial composition, with brown representing pyrolite, white representing harzburgite and green representing basalt. Inset illustrates the mesh and particle distribution.

Rheology

We use a published viscosity profile[29], and our rheology is temperature-dependent using an Arrhenius law, formulated in a way that separates radial and lateral viscosity variations:

$$\eta(r,T) = \eta_0(r) \exp\left(-\frac{H(r)\Delta T}{nRT_{\text{ref}}T}\right) \tag{7}$$

$\eta_0(r)$ is the viscosity profile, and the activation enthalpy $H(r)$ is depth-dependent[29]. T_{ref} is the reference temperature profile (the initial mantle adiabat), $\Delta T = T - T_{\text{ref}}$ the deviation from this adiabat, $n = 1$ is the stress exponent, and $R = 8.314$ J K^{-1} mol^{-1} is the gas constant. Since we only model the lower mantle, we assume that the dominant creep mechanism is diffusion creep. We limit lateral viscosity variations due to temperature to four orders of magnitude, and in addition set a global minimum and maximum viscosity of 10^{19} and 10^{25} Pa s, respectively.

To model the change in viscosity associated with the transition to the ppv phase, we additionally multiply this viscosity by a constant prefactor in the parts of the model where ppv is present. We vary the value of this prefactor as part of our parameter study. Since the look-up tables we use for the equation of state also contain the dominant phase at a given temperature and pressure, we can use them to determine where in the models ppv is stable, depending on the local temperature, pressure and composition (see Figure S7). A sharp viscosity jump at the phase transition, which changes its location with temperature and pressure, would pose challenges for numerical solvers. To avoid these problems, we smooth out the phase transition by solving a diffusion problem with a diffusion length scale of 20 km.

Initial Conditions

The initial mantle temperature follows an adiabat based on a published geotherm[60,61], resulting in a temperature of 2300 K and a pressure of 59.5 GPa at the model top, 1500 km above the CMB. The adiabat is then calculated based on the material properties of pyrolite computed with HeFESTo (see Equation of State). This results in a pressure of 136 GPa at the CMB. Near the CMB, the initial temperature is superadiabatic in a thin thermal boundary layer, computed using a half-space cooling model with a boundary layer age of 10 Myr and a CMB temperature of 3773 K. Furthermore, the temperature deviates from the adiabat at the initial location of the two subducted slabs entering the model. We define the slabs as in a previous study[36], using a Gaussian temperature anomaly with a peak amplitude of -625 K centered at a distance of one third of the slab thickness from the original top of the slab. The width of the Gaussian is a model parameter that we vary together with the thickness of the crust. The initial length of the slabs is 13,000 km, and they enter the model vertically. Prescribing the location and thermal structure of subducted slabs allows us to make slab morphology a model parameter rather than including realistic subduction dynamics in our model, which is a complex problem in itself and goes far beyond the scope of this study.

The initial chemical composition in the model is pyrolitic except for the two subducted slabs. As in a previous study[36], the slabs are assumed to have a basaltic crust and a harzburgitic lithosphere that is 10 times as thick as the crust. Within this lithosphere, the composition changes linearly from 100% harzburgite at the top (where it borders the crust) to 0% harzburgite at the bottom. The crustal thickness is a model parameter varied between 10 and 40 km (and then in turn controls the thickness of the whole slab). Figure 5 shows the initial composition for a crust with 30 km thickness. The reasoning behind a thicker oceanic crust than observed at the Earth's surface is that subducted slabs are expected to thicken on their way from the upper

to the lower mantle by a factor of 2–5[62]. This behavior is visible in seismic tomography[62] and is inferred to be caused by a decrease in slab sinking speed in the lower mantle due to the increase in viscosity with depth[36]. This initial condition relies on a very specific assumption about the slab morphology when transitioning to the lower mantle and does not take into account slab buckling, folding, stagnation, or avalanche events[63], which would lead to a different distribution of crustal material in the lower mantle. We nevertheless use this slab geometry to make our models comparable to previous studies.

Boundary Conditions

The bottom boundary is closed and allows for free slip, while the top boundary is an open boundary with a fixed pressure. Both side boundaries are periodic. We deal with the rotational nullspace introduced by these boundary conditions by setting the net rotation in the model to zero.

The temperature at the bottom boundary is set to 3773 K. At the top boundary, both the temperature and the chemical composition are only prescribed on those parts of the boundary where material flows into the model and are set to the initial conditions in these locations. We let all models evolve for 400 Myrs.

We note that these boundary conditions, together with the slope of the bridgmanite to ppv phase transition given by mineral physics data[3] result in a ubiquitous presence of ppv at the CMB with ppv being stable in hot regions as well. This is consistent with recent experimental data[64].

Table S1 provides a summary of model parameters.

Incompressible models

To determine the impact of the slab density structure on basalt segregation from the slab and to explain discrepancies between previous studies (as outlined in Section Impact of the slab density structure), we created a set of incompressible models using the same density contrasts between basalt, pyrolite and harzburgite as in[35] and[34], and an additional setup using density contrasts based on thermodynamic data[3]. The exact values are listed in Table 1. In these simplified models that also do not include adiabatic heating or shear heating, the phase transition to post-perovskite occurs 300 km above the CMB and has a Clapeyron slope of 7 MPa K^{-1}. We use a constant thermal expansivity of 10^{-5} K^{-1} and a specific heat capacity of 1000 J kg^{-1} K^{-1}. The viscosity follows an Arrhenius viscosity law with a reference temperature of 2500 K at 10^{22} Pa s and an activation enthalpy of 320 kJ mol^{-1}, and is therefore lower than in the more realistic models. The initial mantle temperature profile is set to the reference temperature of 2500 K. All of these parameters are taken from[36]. All other parameters are the same as in our compressible models described above.

Model limitations

Our models rely on a number of assumptions about lower mantle dynamics that limit the conclusions we can draw from them. As outlined in the Initial Conditions section, a more complex slab morphology would alter the distribution of basaltic crust entering the lowermost mantle. In addition, the choice of thermodynamic properties for all mantle materials (which are computed from a mineral physics database[3], but come with uncertainties) affects the balance between buoyancy forces on the one hand, which facilitate segregation and basalt accumulation, and viscous forces on the other hand, which facilitate entrainment of basalt into plumes. This balance is further influenced by using a 2D model geometry, which overemphasizes the effect of entrainment in plumes compared to the 3D Earth[36,65]. Beyond that, the slab sinking speed in our models is determined by the negative buoyancy of the slab alone, whereas on Earth the amount of subducted material that will later enter the lower mantle is likely controlled by the plate configuration and driving and resisting forces in the upper mantle. Therefore, the net inflow of basaltic material into the lower mantle would be independent of the amount of slab thickening, whereas in our models thicker slabs carry basalt into the lower mantle at a higher rate. The main conclusions of our study rely on the general competition between buoyancy and viscous forces and therefore remain valid despite theses limitations. This line of reasoning is also supported by the good agreement with previous studies (see section on Growth of basaltic piles throughout Earth's history in the main text). However, the exact accumulation rates and the values of post-perovskite viscosity and crustal thickness where increased entrainment becomes dominant over increased segregation might be shifted in the Earth compared to our models.

Another important assumption in our models is the ubiquitous presence of ppv in a thin layer above the CMB (see Rheology and Boundary Conditions), which results from the ppv phase transition Clapeyron slope given by the mineral physics data we use[3] (see Figure S7, $\sim$9 MPa K^{-1}) and its assumed anchor point on the adiabat ($\sim$120 GPa and $\sim$2650 K). While there is agreement that the Clapeyron slope is strongly positive, the exact value is still debated and likely depends on the material composition. A larger Clapeyron slope would imply a thinner ppv layer in hot regions, possibly delaying the ascent of plumes while still allowing for the segregation of basaltic material in cold regions. This could lead to a slightly higher rate of basalt accumulation, as discussed in the main text for Earth's past. However, for extreme values of the Clapeyron slope $>$14 MPa K^{-1} (and our CMB temperature of 3773 K), ppv would not be stable directly at the CMB or in hot regions just above. Similarly, higher CMB temperatures or an anchor point with a higher pressure could prevent the ubiquitous presence of ppv above the

CMB. We speculate that this would substantially reduce the plume volume flux and the amount of basalt that plumes would remove from the CMB region and lead to significantly higher rates of basalt accumulation at the CMB, especially for low ppv viscosities.

Table 1. Densities for all compositions in incompressible models, based on different studies. The pyrolitic background is the same for all references with a density of 5000 kg m^{-3} before and 5066.4 kg m^{-3} after the phase transition, and the Δ columns indicate the density difference compared to pyrolite.

Reference	Basalt (kg m^{-3})	Harzburgite (kg m^{-3})	ΔBasalt (kg m^{-3})	ΔHarzburgite (kg m^{-3})
Tackley (2011)	5175 / 5241.4	4950 / 5016.4	175	-50
Li & McNamara (2013)	5128 / 5194.4	– / –	128	–
HeFESTo	5078 / 5144.4	4977 / 5043.4	78	-23

Data availability

We provide all data necessary to reproduce our results as a data publication on Zenodo[66] (https://doi.org/10.5281/zenodo.10067794). This includes ASPECT input files, the results of our model analysis as described in the manuscript (basalt mass, inflow, outflow, accumulation rate, etc.) and the plotting scripts needed to reproduce the diagrams in this manuscript.

Code availability

Our models were run using a modified version of ASPECT 2.4.0-pre (commit c2f3022fb), which is freely available on Github (https://github.com/jdannberg/aspect/tree/ppv_viscosity_smoothed). We utilized the libraries deal.II[67], Trilinos[68], and p4est[69], and we created our figures using ParaView[70], python/matplotlib[71] and Inkscape.

References

1. Hirose, K., Fei, Y., Ma, Y. & Mao, H.-K. The fate of subducted basaltic crust in the earth's lower mantle. *Nature* **397**, 53–56 (1999).
2. Hirose, K., Takafuji, N., Sata, N. & Ohishi, Y. Phase transition and density of subducted morb crust in the lower mantle. *Earth Planet. Sci. Lett.* **237**, 239–251 (2005).
3. Stixrude, L. & Lithgow-Bertelloni, C. Thermodynamics of mantle minerals - II. Phase equilibria. *Geophys. J. Int.* **184**, 1180–1213, DOI: 10.1111/j.1365-246X.2010.04890.x (2011).
4. Hofmann, A. W. & White, W. M. Mantle plumes from ancient oceanic crust. *Earth Planet. Sci. Lett.* **57**, 421–436 (1982).
5. Li, M. The cycling of subducted oceanic crust in the Earth's deep mantle. In *Mantle Convection and Surface Expressions*, 303–328, DOI: 10.1002/9781119528609.ch12 (Wiley Online Library, 2021).
6. Sobolev, A. V., Hofmann, A. W., Sobolev, S. V. & Nikogosian, I. K. An olivine-free mantle source of Hawaiian shield basalts. *Nature* **434**, 590–597 (2005).
7. Sobolev, A. V. *et al.* The amount of recycled crust in sources of mantle-derived melts. *Science* **316**, 412–417 (2007).
8. Sobolev, S. V. *et al.* Linking mantle plumes, large igneous provinces and environmental catastrophes. *Nature* **477**, 312–316 (2011).
9. Cabral, R. A. *et al.* Anomalous sulphur isotopes in plume lavas reveal deep mantle storage of Archaean crust. *Nature* **496**, 490–493 (2013).
10. Koppers, A. A. *et al.* Mantle plumes and their role in earth processes. *Nat. Rev. Earth & Environ.* **2**, 382–401 (2021).
11. Sobolev, A. V., Hofmann, A. W., Jochum, K. P., Kuzmin, D. V. & Stoll, B. A young source for the hawaiian plume. *Nature* **476**, 434–437 (2011).
12. Wang, X.-C. *et al.* Identification of an ancient mantle reservoir and young recycled materials in the source region of a young mantle plume: Implications for potential linkages between plume and plate tectonics. *Earth Planet. Sci. Lett.* **377**, 248–259 (2013).

13. Delavault, H., Chauvel, C., Sobolev, A. & Batanova, V. Combined petrological, geochemical and isotopic modeling of a plume source: Example of gambier island, pitcairn chain. *Earth Planet. Sci. Lett.* **426**, 23–35 (2015).

14. Garnero, E. J., McNamara, A. K. & Shim, S.-H. Continent-sized anomalous zones with low seismic velocity at the base of earth's mantle. *Nat. Geosci.* **9**, 481–489 (2016).

15. McNamara, A. K. A review of large low shear velocity provinces and ultra low velocity zones. *Tectonophysics* **760**, 199–220 (2019).

16. Romanowicz, B. Can we resolve 3d density heterogeneity in the lower mantle? *Geophys. research letters* **28**, 1107–1110 (2001).

17. Deschamps, F. & Trampert, J. Mantle tomography and its relation to temperature and composition. *Phys. Earth Planet. Interiors* **140**, 277–291 (2003).

18. Hernlund, J. W. & Houser, C. On the statistical distribution of seismic velocities in earth's deep mantle. *Earth Planet. Sci. Lett.* **265**, 423–437 (2008).

19. Lekic, V., Cottaar, S., Dziewonski, A. & Romanowicz, B. Cluster analysis of global lower mantle tomography: A new class of structure and implications for chemical heterogeneity. *Earth Planet. Sci. Lett.* **357**, 68–77 (2012).

20. He, Y. & Wen, L. Geographic boundary of the "pacific anomaly" and its geometry and transitional structure in the north. *J. Geophys. Res. Solid Earth* **117** (2012).

21. Zhao, C., Garnero, E. J., McNamara, A. K., Schmerr, N. & Carlson, R. W. Seismic evidence for a chemically distinct thermochemical reservoir in earth's deep mantle beneath hawaii. *Earth Planet. Sci. Lett.* **426**, 143–153 (2015).

22. Koelemeijer, P., Ritsema, J., Deuss, A. & Van Heijst, H.-J. Sp12rts: a degree-12 model of shear-and compressional-wave velocity for earth's mantle. *Geophys. J. Int.* **204**, 1024–1039 (2016).

23. Trampert, J., Deschamps, F., Resovsky, J. & Yuen, D. Probabilistic tomography maps chemical heterogeneities throughout the lower mantle. *Science* **306**, 853–856 (2004).

24. Lau, H. C. *et al.* Tidal tomography constrains earth's deep-mantle buoyancy. *Nature* **551**, 321–326 (2017).

25. Thorne, M. S., Garnero, E. J. & Grand, S. P. Geographic correlation between hot spots and deep mantle lateral shear-wave velocity gradients. *Phys. Earth Planet. Interiors* **146**, 47–63 (2004).

26. Torsvik, T. H., Smethurst, M. A., Burke, K. & Steinberger, B. Large igneous provinces generated from the margins of the large low-velocity provinces in the deep mantle. *Geophys. J. Int.* **167**, 1447–1460 (2006).

27. Burke, K., Steinberger, B., Torsvik, T. H. & Smethurst, M. A. Plume generation zones at the margins of large low shear velocity provinces on the core–mantle boundary. *Earth Planet. Sci. Lett.* **265**, 49–60 (2008).

28. Mitrovica, J. & Forte, A. A new inference of mantle viscosity based upon joint inversion of convection and glacial isostatic adjustment data. *Earth Planet. Sci. Lett.* **225**, 177–189 (2004).

29. Steinberger, B. & Calderwood, A. R. Models of large-scale viscous flow in the Earth's mantle with constraints from mineral physics and surface observations. *Geophys. J. Int.* **2**, 1461–1481, DOI: 10.1111/j.1365-246X.2006.03131.x (2006).

30. Čížková, H., van den Berg, A. P., Spakman, W. & Matyska, C. The viscosity of Earth's lower mantle inferred from sinking speed of subducted lithosphere. *Phys. earth Planet. Interiors* **200**, 56–62 (2012).

31. Hunt, S. A. *et al.* Weakening of calcium iridate during its transformation from perovskite to post-perovskite. *Nat. Geosci.* **2**, 794–797 (2009).

32. Ammann, M., Brodholt, J., Wookey, J. & Dobson, D. First-principles constraints on diffusion in lower-mantle minerals and a weak D" layer. *Nature* **465**, 462–465 (2010).

33. Goryaeva, A. M., Carrez, P. & Cordier, P. Low viscosity and high attenuation in MgSiO3 post-perovskite inferred from atomic-scale calculations. *Sci. reports* **6**, 1–10 (2016).

34. Li, M. & McNamara, A. K. The difficulty for subducted oceanic crust to accumulate at the Earth's core-mantle boundary. *J. Geophys. Res. Solid Earth* **118**, 1807–1816, DOI: 10.1002/jgrb.50156 (2013).

35. Nakagawa, T. & Tackley, P. J. Effects of low-viscosity post-perovskite on thermo-chemical mantle convection in a 3-D spherical shell. *Geophys. Res. Lett.* **38**, 1–6, DOI: 10.1029/2010GL046494 (2011).

36. Tackley, P. J. Living dead slabs in 3-D: The dynamics of compositionally-stratified slabs entering a "slab graveyard" above the core-mantle boundary. *Phys. Earth Planet. Interiors* **188**, 150–162, DOI: 10.1016/j.pepi.2011.04.013 (2011).

37. Li, M., McNamara, A. K. & Garnero, E. J. Chemical complexity of hotspots caused by cycling oceanic crust through mantle reservoirs. *Nat. Geosci.* **7**, 366–370 (2014).

38. Li, M. & McNamara, A. K. Evolving morphology of crustal accumulations in earth's lowermost mantle. *Earth Planet. Sci. Lett.* **577**, 117265 (2022).

39. Li, Y., Deschamps, F. & Tackley, P. J. Effects of low-viscosity post-perovskite on the stability and structure of primordial reservoirs in the lower mantle. *Geophys. Res. Lett.* **41**, 7089–7097 (2014).

40. Schubert, G., Turcotte, D. L. & Olson, P. *Mantle Convection in the Earth and Planets, Part 1* (Cambridge, 2001).

41. Davaille, A., Girard, F. & Le Bars, M. How to anchor hotspots in a convecting mantle? *Earth Planet. Sci. Lett.* **203**, 621–634 (2002).

42. Vogt, P. Asthenosphere motion recorded by the ocean floor south of iceland. *Earth Planet. Sci. Lett.* **13**, 153–160 (1971).

43. White, R., Bown, J. & Smallwood, J. The temperature of the iceland plume and origin of outward-propagating v-shaped ridges. *J. Geol. Soc.* **152**, 1039–1045 (1995).

44. Jones, S. M., White, N. & Maclennan, J. V-shaped ridges around iceland: Implications for spatial and temporal patterns of mantle convection. *Geochem. Geophys. Geosystems* **3**, 1–23 (2002).

45. Parnell-Turner, R. *et al.* A continuous 55-million-year record of transient mantle plume activity beneath iceland. *Nat. Geosci.* **7**, 914–919 (2014).

46. Cottaar, S. & Lekic, V. Morphology of seismically slow lower-mantle structures. *Geophys. Suppl. to Mon. Notices Royal Astron. Soc.* **207**, 1122–1136 (2016).

47. Herzberg, C., Condie, K. & Korenaga, J. Thermal history of the earth and its petrological expression. *Earth Planet. Sci. Lett.* **292**, 79–88 (2010).

48. Nakagawa, T. & Tackley, P. J. Effects of thermo-chemical mantle convection on the thermal evolution of the earth's core. *Earth Planet. Sci. Lett.* **220**, 107–119 (2004).

49. Li, M. & McNamara, A. K. The influence of deep mantle compositional heterogeneity on earth's thermal evolution. *Earth Planet. Sci. Lett.* **500**, 86–96 (2018).

50. Kronbichler, M., Heister, T. & Bangerth, W. High accuracy mantle convection simulation through modern numerical methods. *Geophys. J. Int.* **191**, 12–29 (2012).

51. Heister, T., Dannberg, J., Gassmöller, R. & Bangerth, W. High accuracy mantle convection simulation through modern numerical methods. II: Realistic models and problems. *Geophys. J. Int.* **210**, 833–851, DOI: 10.1093/gji/ggx195 (2017).

52. Gassmöller, R., Lokavarapu, H., Heien, E., Puckett, E. G. & Bangerth, W. Flexible and scalable particle-in-cell methods with adaptive mesh refinement for geodynamic computations. *Geochem. Geophys. Geosystems* **19**, 3596–3604, DOI: 10.1029/2018GC007508 (2018).

53. He, Y., Puckett, E. G. & Billen, M. I. A discontinuous Galerkin method with a bound preserving limiter for the advection of non-diffusive fields in solid earth geodynamics. *Phys. Earth Planet. Interiors* **263**, 23 – 37, DOI: 10.1016/j.pepi.2016.12.001 (2017).

54. Clevenger, T. C. & Heister, T. Comparison between algebraic and matrix-free geometric multigrid for a stokes problem on adaptive meshes with variable viscosity. *Numer. Linear Algebr. with Appl.* **28**, e2375 (2021).

55. Gassmöller, R., Lokavarapu, H., Bangerth, W. & Puckett, E. G. Evaluating the accuracy of hybrid finite element/particle-in-cell methods for modelling incompressible Stokes flow. *Geophys. J. Int.* **219**, 1915–1938, DOI: 10.1093/gji/ggz405 (2019). https://academic.oup.com/gji/article-pdf/219/3/1915/30105955/ggz405.pdf.

56. Stixrude, L. & Lithgow-Bertelloni, C. Thermodynamics of mantle minerals–I. Physical properties. *Geophys. J. Int.* **162**, 610–632 (2005).

57. Stixrude, L. & Lithgow-Bertelloni, C. Thermal expansivity, heat capacity and bulk modulus of the mantle. *Geophys. J. Int.* **228**, 1119–1149 (2022).

58. Xu, W., Lithgow-Bertelloni, C., Stixrude, L. & Ritsema, J. The effect of bulk composition and temperature on mantle seismic structure. *Earth Planet. Sci. Lett.* **275**, 70–79 (2008).

59. Stackhouse, S., Stixrude, L. & Karki, B. B. First-principles calculations of the lattice thermal conductivity of the lower mantle. *Earth Planet. Sci. Lett.* **427**, 11–17 (2015).

60. Maeda, F. *et al.* Diamond formation in the deep lower mantle: a high-pressure reaction of MgCO3 and SiO2. *Sci. Reports* **7**, 40602, DOI: 10.1038/srep40602 (2017).

61. Katsura, T., Yoneda, A., Yamazaki, D., Yoshino, T. & Ito, E. Adiabatic temperature profile in the mantle. *Phys. Earth Planet. Interiors* **183**, 212–218, DOI: 10.1016/j.pepi.2010.07.001 (2010).

62. Goes, S., Agrusta, R., van Hunen, J. & Garel, F. Subduction-transition zone interaction: A review. *Geosphere* **13**, 644–664 (2017).

63. Garel, F. *et al.* Interaction of subducted slabs with the mantle transition-zone: A regime diagram from 2-d thermo-mechanical models with a mobile trench and an overriding plate. *Geochem. Geophys. Geosystems* **15**, 1739–1765 (2014).

64. Kuwayama, Y. *et al.* Post-perovskite phase transition in the pyrolitic lowermost mantle: Implications for ubiquitous occurrence of post-perovskite above CMB. *Geophys. Res. Lett.* **49**, e2021GL096219 (2022).

65. Davies, G. F. Stirring geochemistry in mantle convection models with stiff plates and slabs. *Geochimica et Cosmochimica Acta* **66**, 3125–3142 (2002).

66. Dannberg, J., Chotalia, K. & Gassmöller, R. How lowermost mantle viscosity controls the chemical structure of Earth's deep interior: Data, DOI: 10.5281/zenodo.10067794 (2023).

67. Arndt, D. *et al.* The deal.ii library, version 9.4. *J. Numer. Math.* **30**, 231–246, DOI: doi:10.1515/jnma-2022-0054 (2022).

68. Trilinos Project Team, T. *The Trilinos Project Website* (2020 (acccessed May 22, 2020)).

69. Burstedde, C., Wilcox, L. C. & Ghattas, O. `p4est`: Scalable algorithms for parallel adaptive mesh refinement on forests of octrees. *SIAM J. on Sci. Comput.* **33**, 1103–1133, DOI: 10.1137/100791634 (2011).

70. Ahrens, J., Geveci, B. & Law, C. ParaView: An end-user tool for large data visualization. In *Visualization Handbook* (Elesvier, 2005). ISBN 978-0123875822.

71. Hunter, J. D. Matplotlib: A 2D graphics environment. *Comput. Sci. & Eng.* **9**, 90–95, DOI: 10.1109/MCSE.2007.55 (2007).

Acknowledgements

We thank Lars Stixrude and Carolina Lithgow-Bertelloni for the development of HeFESTo and for providing the look-up tables of material properties used in this study. We thank the Computational Infrastructure for Geodynamics (geodynamics.org) which is funded by the National Science Foundation under award EAR-0949446, EAR-1550901, and EAR-2149126 for supporting RG and the development of ASPECT. JD and RG were partially supported by the NSF grants EAR-1925677 and EAR-2054605. The authors also acknowledge University of Florida Research Computing (https://www.rc.ufl.edu/) for providing computational resources and support that have contributed to the research results reported in this publication.

Author contributions statement

J.D. and K.C. designed research, performed research, and analyzed data. All authors (J.D., K.C. and R.G.) developed numerical methods and wrote the paper.

Competing interests

The authors declare no competing interests.